Chemical Physics 152 (1991) 241–259
North-Holland

Avoided-crossing molecular-beam study of the torsion–rotation energy levels of CH_3CF_3

W. Leo Meerts
Fysisch Laboratorium, University of Nijmegen, Toernooiveld, 6525 ED Nijmegen, The Netherlands

and

Irving Ozier
Department of Physics, University of British Columbia, 6224 Agriculture Road, Vancouver BC, Canada V6T 2A6

Received 22 October 1990

The avoided-crossing molecular-beam electric resonance method has been used to determine the leading parameters in the torsion–rotation Hamiltonian of CH_3CF_3, which was selected as a prototype for the case of a symmetric rotor with small ($\leqslant 500$ kHz) internal rotor splittings. Stark anticrossings have been studied for ($K=\pm 2 \leftrightarrow \mp 1$) with $J=2$–6; hyperfine anticrossings have been studied for ($K=\pm 2 \leftrightarrow 0$), ($\pm 2 \leftrightarrow \pm 1$), and ($\pm 1 \leftrightarrow 0$) with $J \leqslant 2$. A detailed investigation of the hyperfine case has been carried out involving selection rules, relative intensity calculations, Zeeman studies, and combination differences. Several pure rotational transitions for the lowest two torsional states have been measured between 93 and 114 GHz with a mm-wave spectrometer. The ($J=1 \leftarrow 0$) transition in the ground torsional state has been measured with the molecular beam spectrometer. Stark and Zeeman studies have been carried out with conventional molecular beam techniques. It has been determined that the effective rotational constant $A^{\rm eff}=5502.904(3)$ MHz, the effective height of the threefold barrier to internal rotation $V^{\rm eff}=1093(11)$ cm^{-1} and the moment of inertia of the methyl top $I_\alpha=3.21(4)$ amu Å^2. It has been found that the electric dipole moment $\mu=2.34720(13)$ D and the distortion dipole moment constant $\mu_{\rm D}=3.220(11)$ μD. The magnitudes and signs of the molecular g-factors have been obtained: $g_\parallel=-0.0226(13)$ nm and $g_\perp=-0.117(1)$ nm. In addition, values have been determined for the B-rotational constant and several distortion constants.

1. Introduction

The avoided-crossing method of studying internal rotation in symmetric tops is now well established [1]. Conventional microwave spectroscopy cannot provide precision values for the leading torsional terms in the Hamiltonian of a symmetric rotor because these terms are conserved in the allowed dipole transitions. However, the anticrossing method breaks many of these selection rules and provides, in favourable cases, for the determination of the height V_3 of the three-fold barrier to internal rotation, the moment of inertia I_a of the molecule about the symmetry axis, and the corresponding moment of inertia I_α of the top undergoing the torsional oscillations.

The anticrossings can be classified according to two different characteristics. When classified in terms of the mechanism which mixes the two levels that interact in the crossing region, the avoided crossings are labelled "Stark" or "hyperfine". In the Stark case, the mixing matrix element η arises from the distortion dipole moment $\mu_{\rm D}$ [2,3]. The selection rules are $\Delta J=0, \pm 1$; $\Delta K=\pm 3$; $\Delta\sigma=0$; $\Delta m_J=0, \pm 1$. Here K and m_J, respectively, are the eigenvalues of the components of the rotational angular moment $\boldsymbol{J}$ along the symmetry axis and the external static electric field $\boldsymbol{\epsilon}$ [#1]. The index $\sigma=0, \pm 1$ labels the three torsional sublevels for each value of the principal torsional quantum number v. In the hyperfine case, η arises from the internal interactions involving the nuclear spins

[#1] The symbol ϵ has been used throughout this paper to indicate the electric field. We have chosen ϵ rather than E to avoid confusion with the energy.

0301-0104/91/$ 03.50 © 1991 – Elsevier Science Publishers B.V. (North-Holland)

in the top and the frame. A list of the selection rules for the spin–spin and spin–rotation interactions includes $\Delta J=0, \pm 1; \Delta K=0, \pm 1, \pm 2; \Delta m_J=0, \pm 1, \pm 2$.

When the anticrossings are classified in terms of the type of energy that is changed in the corresponding zero-field transition, the cases are labelled "barrier" or "rotational". In the former, the energy of rigid rotation is conserved ($\Delta|K|=0$); in the latter, it is not conserved ($\Delta|K|\neq 0$).

Following a preliminary study of CH_3CF_3 [4], detailed investigations were carried out for CH_3SiH_3 [5], CH_3SiF_3 [6], and CH_3CD_3 [7]. For each of the three molecules studied in detail, the barrier anticrossings could be observed. If the A-rotational constant is known, then the barrier type of anticrossing by itself can be used to get V_3 and I_α. However, for a molecule with a high barrier and a large dipole moment μ, the crossing fields for the barrier avoided crossings are so low that the associated spectra are obscured by the normal Stark transitions. This will be called the high barrier case. CH_3CF_3 falls in this category.

For such cases, the determination of V_3 and I_α must be made from rotational anticrossings. In the high barrier limit, the Stark anticrossings for ($K=\pm 2 \leftrightarrow \mp 1$) yield a symmetric triplet which provides only a single constraint on V_3 and I_α [4]. The hyperfine avoided crossings provide a second constraint. However, unlike the barrier and the Stark rotational cases, the crossing fields for the hyperfine rotational cases are subject to shifts from the diagonal terms in the high barrier hyperfine Hamiltonian. As a result, precision studies of high barrier molecules have not been previously carried out. It is the purpose of the current work to use CH_3CF_3 as a prototype for such a precision study.

Two recent investigations have laid the foundation for a good deal of the present work. In the first, the lineshape function for a transition in a molecule with a linear Stark effect was derived [8]. In the second, the detailed selection rules for the spin rotation and classical spin–spin interactions were obtained and the matrix elements were calculated [9]. These two works made it possible to predict the relative intensities of the different anticrossing signals for the case where the spin–spin terms dominate. The present study of CH_3CF_3 provides a test of some these predictions.

The current work is divided into nine sections. In section 2, the theoretical background is presented. The torsion–rotation and nuclear hyperfine Hamiltonians are discussed with emphasis on the selection rules for the hyperfine terms that break the torsion–rotation symmetry. The basis is laid for relative intensity calculations by discussing the two-level transition probability for the case where a large linear Stark effect must be taken into account. Section 3 describes the experimental methods and conditions for the beam studies. Section 4 presents the measurement of the rotational spectrum by both mm-wave absorption and molecular beam spectroscopy. In addition, section 4 presents the measurement of the electric dipole moment.

Sections 5 and 6 describe the anticrossing spectra and the preliminary analysis for the Stark and hyperfine cases, respectively. The hyperfine anticrossing studies involved arguments concerning selection rules, relative intensities, effective g-factors, and combination differences. Section 7 deals with the determination of the torsion–rotation parameters.

Section 8 presents a series of studies on related subjects: the J-dependence of the effective dipole moment, the distortion dipole moment, and the magnitude and signs of the molecular g-factors. Finally, section 9 summarizes the results of the current work and discusses some of the implications for other investigations.

The determinations made here of the various molecular parameters in CH_3CF_3 are given in table 1.

2. Theory

2.1. Torsion–rotation Hamiltonian

The torsion–rotation Hamiltonian H_{TR} has been discussed in detail in connection with various studies of CH_3SiH_3 [5,10,11]. Here we shall introduce only the terms relevant to the current study. In the internal axis method (IAM), H_{TR} can be formally written as

$$H_{TR}=H_{TR}^{(0)}+H_{TR}^{(1)}. \tag{1}$$

In zeroth order in the IAM, the rotational and torsional degrees of freedom are completely decoupled and

Table 1
Molecular constants for CH_3CF_3

Quantity	Units	Value
$\mu/\mu(\mathrm{OCS})$ [a]		3.281928(64)
μ [a]	D	2.34720(13)
μ_J [b]	10^{-6} D	−0.66(20)
μ_D	10^{-6} D	3.220(11)
$g_\parallel$	nm	−0.0226(3)
$g_\perp$	nm	−0.0177(1)
A^{eff}	MHz	5502.904(3)
B	MHz	5189.176(2)
D_J	kHz	1.278(9)
D_{JK}	kHz	1.983(12)
ρ		0.0349(4)
V_3^{eff}	cm^{-1}	1093(11)
F_{3J}^{eff}	MHz	−76.17(3)

[a] Here μ represents the dipole moment in the $J_K=3_{\pm 2}$ state.
[b] The sign of μ_J is defined relative to that of μ_0.

$$H_{\mathrm{TR}}^{(0)} = B\boldsymbol{J}^2 + (A-B)J_z^2 + F\boldsymbol{p}^2 + V_3\tfrac{1}{2}(1-\cos 3\alpha)\,. \tag{2}$$

The first two terms form the Hamiltonian $H_{\mathrm{R}}^{(0)}$ for rigid rotation, while the last two form the pure torsional Hamiltonian $H_{\mathrm{T}}^{(0)}$, J_z and $\boldsymbol{p}$ are, respectively, the rotational and torsional angular momenta about the symmetry axis. The angle α measures the torsional displacement of the CH_3 top from the staggered configuration relative to the CF_3 frame. The reduced rotational constant $F=A/[\rho(1-\rho)]$, where $\rho=I_\alpha/I_a$.

Here the first-order Hamiltonian $H_{\mathrm{TR}}^{(1)}$ can be taken as

$$\begin{aligned} H_{\mathrm{TR}}^{(1)} = &-D_J\boldsymbol{J}^4 - D_{JK}\boldsymbol{J}^2J_z^2 - D_KJ_z^4 \\ &- [D_{Jm}\boldsymbol{p}^2 - F_{3J}\tfrac{1}{2}(1-\cos 3\alpha)]\,\boldsymbol{J}^2 \\ &- [D_{Km}\boldsymbol{p}^2 - F_{3K}\tfrac{1}{2}(1-\cos 3\alpha)]\,J_z^2\,. \end{aligned} \tag{3}$$

The first three terms are the usual quartic centrifugal distortion contributions. The remaining terms arise from quartic torsion–rotation interactions.

Several of the constants in H_{TR} must be considered to be effective parameters because of the truncation of the Hamiltonian. A detailed discussion of the effective parameters and the difficulties in separating them is given elsewhere [10,11].

2.2. The nuclear hyperfine interactions

The nuclear hyperfine Hamiltonian H_{HYP} for molecules such as CH_3CF_3 has been the subject recently of a detailed theoretical investigation [9]. This Hamiltonian can be expressed in terms of $\boldsymbol{J}$, the resultant vector $\boldsymbol{I}_{\mathrm{T}}$ for the three hydrogen spins in the top, and the resultant vector $\boldsymbol{I}_{\mathrm{F}}$ for the three fluorine spins in the frame. Here we shall discuss briefly the relevant terms in H_{HYP} with emphasis on the selection rules.

The nuclear hyperfine Hamiltonian can be formally written as

$$H_{\mathrm{HYP}} = H_{\mathrm{T}J} + H_{\mathrm{F}J} + H_{\mathrm{TT}} + H_{\mathrm{FF}} + H_{\mathrm{TF}}\,. \tag{4}$$

Here $H_{\mathrm{T}J}$ and $H_{\mathrm{F}J}$ are the spin–rotation interactions of $\boldsymbol{J}$ with $\boldsymbol{I}_{\mathrm{T}}$ and $\boldsymbol{I}_{\mathrm{F}}$, respectively. The three remaining terms in eq. (4) are the three possible spin–spin Hamiltonians: H_{TT} for the top–top coupling, H_{FF} for the frame–frame coupling, and H_{TF} for top–frame interaction. Each spin–spin term includes only the classical contribution, so that it is a second rank tensor with a coupling constant that can be calculated from the structure. The electron-coupled terms are expected to be small and are not considered here. The spin–torsion interactions of the torsional angular momentum $\boldsymbol{p}$ with $\boldsymbol{I}_{\mathrm{T}}$ and $\boldsymbol{I}_{\mathrm{F}}$ are also negligible.

The wavefunctions used to calculate the Hamiltonian matrix are in the high-field representation appropriate to the anticrossing experiments. A large static electric field ϵ is assumed to be in the space-fixed Z-direction. A static magnetic field $\boldsymbol{B}$ is assumed to be parallel to ϵ and to have a magnitude $\geqslant 2$ mT. The representation is characterized by the quantum numbers $\Lambda \equiv (vJK\sigma m_J; I_{\mathrm{T}}m_{\mathrm{T}}I_{\mathrm{F}}m_{\mathrm{F}})$. Here m_{T} and m_{F} are, respectively, the eigenvalues of the Z-components of $\boldsymbol{I}_{\mathrm{T}}$ and $\boldsymbol{I}_{\mathrm{F}}$. The Hamiltonian is, of course, diagonal in the magnetic quantum number m_{TOT} of the total angular momentum: $m_{\mathrm{TOT}} = m_J + m_{\mathrm{T}} + m_{\mathrm{F}}$. For a detailed description of the role played by ϵ and $\boldsymbol{B}$ in determining the representation, see section 4.A of ref. [9] and section 2.A of ref. [12].

The symmetries of the *different* parts of the total wave function in the IAM are discussed in terms of the extended permutation-inversion group $G_8^{(m)}$ by Hougen et al. [9]. In this group-theoretical approach, ρ is approximated by the rational fraction p/m, where the integers p and m can be as large as the

experimental accuracy requires. The torsion–rotation symmetry Γ_{RT} can be properly defined in IAM for the unextended molecular group G_{18} [9,13]. This symmetry is given as a function of (v, J, K, σ) in table II of ref. [14].

In order to discuss the selection rules, we represent the five terms in eq. (4) in turn from left to right by $H^{(i)}_{HYP}$, $i=1, 2, ..., 5$. The matrix elements of interest can then be written formally as $\langle \Lambda_\alpha | H^{(i)}_{HYP} | \Lambda_\beta \rangle$. In accordance with the convention adopted in [12], the indices α and β, respectively, label the upper and lower states when ϵ is much smaller than the crossing field ϵ_c. It is convenient to write each matrix element as the product of a torsional (T), rotational (R) and nuclear spin (N) factor:

$$\langle \Lambda_\alpha | H^{(i)}_{HYP} | \Lambda_\beta \rangle = \langle \Lambda^T_\alpha | H^{(T,i)}_{HYP} | \Lambda^T_\beta \rangle \times \langle \Lambda^R_\alpha | H^{(R,i)}_{HYP} | \Lambda^R_\beta \rangle \langle \Lambda^N_\alpha | H^{(N,i)}_{HYP} | \Lambda^N_\beta \rangle , \quad (5)$$

where $|\Lambda^T\rangle = |vK\sigma\rangle$; $|\Lambda^R\rangle = |JKm_J\rangle$; $|\Lambda^N\rangle = |I_T m_T I_F m_F\rangle$.

The selection rules of particular interest are those on K and σ. In the left hand column of tables IX–XII of ref. [9], the five nuclear hyperfine interactions $H^{(i)}_{HYP}$ are given in terms of IAM "nuclear spin" operators. Because the operators are in the IAM, they act on both the rotational and nuclear spin degrees of freedom. However, they do not act on the torsional part of the wavefunction; see eq. (13) of ref. [9]. The entire α-dependence is shown explicitly in these tables and can be used directly to deduce the (K, σ) selection rules for the torsional matrix element in eq. (5).

The α-dependence of the hyperfine interactions in the IAM takes the form $e^{3ni\alpha}\, e^{iq\alpha}\, e^{irp\alpha}$, where n is any positive or negative integer, $q=-1, 0, +1$, and $r=-2, -1, 0, +1, +2$. The p/m in the tables of ref. [9] has here been replaced by ρ. The factor $e^{3ni\alpha}$ provides for the Fourier decomposition of the α-dependent function which is present in the particular $H^{(i)}_{HYP}$ under consideration. The factor $e^{iq\alpha}$ (together with $e^{3ni\alpha}$ if $n \neq 0$) acts as a ladder operator on σ and gives the σ-selection rule. For example, $e^{-i\alpha}$ gives $\Delta\sigma \equiv \sigma_\alpha - \sigma_\beta = -1$ with $n=0$ and $\Delta\sigma = +2$ with $n=1$. The factor $e^{irp\alpha}$ acts as a ladder operator in K and gives the K-selection rule. For example, $e^{+i2\rho\alpha}$ gives $\Delta K \equiv K_\alpha - K_\beta = -2$. The K- and σ-selection rules for the torsional factor of each $H^{(i)}_{HYP}$ are given in table 2. These can then be used to deduce the allowed changes in the torsional–rotation symmetry Γ_{RT}.

The selection rules on J, m_J, m_T, and m_F follow from angular momentum arguments applied to the rotational and nuclear spin factors in eq. (5). For example, the spin–rotation interactions involve only first-rank operators in $\boldsymbol{J}$ and so $\Delta m_J = 0, \pm 1$, while the spin–spin interactions involve second-rank operators in $\boldsymbol{J}$ and so Δm_J in this case is $0, \pm 1, \pm 2$. A full list of the selection rules is not given here.

There are two similar situations in which the nuclear spin factor in eq. (5) provides an additional constraint on ΔK beyond those listed in table 2. These involve H_{TT} and H_{FF}. Consider H_{TT} first. Here $\Delta m_F = 0$. Since $\Delta m_{TOT} = 0$, we have $\Delta m_T = -\Delta m_J$. If $|\Delta m_J| = 2$, then $|\Delta m_T| = 2$. However, if $I^\alpha_T = I^\beta_T = \frac{1}{2}$, $|\Delta m_T| \leq 1$. In this case, the associated ΔK becomes forbidden. A similar situation arises for H_{FF}. This does not happen for H_{TF} because $|\Delta m_J| = 2$ implies that both m_T and m_F change by a single unit. Argu-

Table 2
(K, σ) selection rules for the torsional factor in the nuclear hyperfine IAM matrix elements [a]

ΔK	$\Delta\sigma$				
	H_{TJ}	H_{FJ}	H_{FF}	H_{TT}	H_{TF}
+2	−1, +2	0	0	−1, +2	0, +1, −2, −1, +2
+1	+1, −2	0	x [b]	x [b]	0, +1, −2, −1, +2
0	0	0	0	0	0, +1, −2, −1, +2
−1	−1, +2	0	x [b]	x [b]	0, +1, −2, −1, +2
−2	+1, −2	0	0	+1, −2	0, +1, −2, −1, +2

[a] The same selection rules apply to the overall hyperfine matrix elements with a few exceptions, which arise from H_{FF} and H_{TT}. In these exceptional cases, further restrictions on ΔK are produced by the nuclear spin matrix elements. See section 2.2.
[b] These matrix elements vanish.

ments similar to those used here for H_{TT} and H_{FF} lead to the conclusion that, in OPF_3 for example, the ($\Delta K=0$) matrix elements vanish for the fluorine–fluorine dipolar interaction if $K/3$ is not an integer [15].

The most striking result in table 2 is the fact that H_{TT} and H_{FF} will not couple levels with $\Delta K=\pm 1$, whereas H_{TF} will do so. A similar result was obtained for C_{3v} molecules. For OPF_3, the fluorine–fluorine classical dipolar interaction does not allow $\Delta K=\pm 1$, whereas the phosphorus–fluorine interaction does allow $\Delta K=\pm 1$. See table 3 of ref. [12]. This table also provides a useful comparison for the other selection rules.

2.3. The transition probabilities

The peak intensity of the resonance signal for the anticrossing $\Lambda_\alpha \leftrightarrow \Lambda_\beta$ is proportional to the on-resonance transition probability denoted here by P_0. For most of the cases of interest under the experimental conditions used here, the two levels Λ_α and Λ_β can be treated as an isolated two-level system. In the standard treatment [16] of the two-level problem, P_0 can always be made unity (at least in principle) by increasing the amplitude ϵ_{RF} of the oscillating electric field driving the transition. However, because of the ac Stark effect, the two-level treatment must be modified if the energy difference between the two states varies linearly with the electric field [8], and, in some cases, P_0 cannot be made unity by varying ϵ_{RF}. The modified two-level problem has been considered recently both for the general case and for the specific case of an avoided crossing [8]. The analysis developed will be applied here.

The on-resonance transition probability can be written in general as

$$P_0=\{\sin y_0\}^2. \tag{6}$$

When the resonance frequency ν_0 is much larger than the minimum energy separation ν_m that exists at the crossing field ϵ_c, we can, to excellent approximation, write

$$y_0=2\pi\eta t J_1(z_0)\,; \tag{7a}$$

$$z_0=|\Delta\mu_{\alpha\beta}\epsilon_{RF}/h\nu_0|\,. \tag{7b}$$

Here η is the matrix element (in Hz) mixing the levels Λ_α and Λ_β, while t is the transit time through the oscillating field. J_1 is the first-order Bessel function [17]. It takes its maximum value $(J_1)_{max}$ of 0.58187 when its argument takes the value $(z_0)_{max}$ of 1.841. $\Delta\mu_{\alpha\beta}$ is the derivative of the transition frequency with respect to $(\epsilon-\epsilon_c)$ when only the linear Stark effect is taken into account. Since all the avoided crossings of interest here have $J_\alpha=J_\beta=J$,

$$\Delta\mu_{\alpha\beta}=\mu(K_\alpha m_J^\alpha-K_\beta m_J^\beta)/J(J+1)\,. \tag{8}$$

For a given value of t, there exists for $|\eta|$ a threshold value $|\eta_T|$ that divides the dependence of P_0 on ϵ_{RF} into two regimes. This threshold is defined by:

$$|\eta_T|=1/[4t(J_1)_{max}]\,. \tag{9}$$

When $y_0=\frac{1}{2}\pi$, $P_0=1$. However, below threshold when $|\eta|<|\eta_T|$, $(J_1)_{max}$ is too small to permit y_0 to meet this "$\frac{1}{2}\pi$ condition", and the maximum value of P_0 is less than unity. In this case, the value ϵ_{RF}^{OPT} of rf amplitude ϵ_{RF} which maximizes P_0 is given by eq. (7b) with $z_0=(z_0)_{max}$. As long as $|\eta|<|\eta_T|$, ϵ_{RF}^{OPT} depends only on $\Delta\mu_{\alpha\beta}$ and on ν_0. On the other hand, above threshold when $|\eta|\geq|\eta_T|$, the $\frac{1}{2}\pi$ condition can be met and the value of ϵ_{RF}^{OPT} is given by eq. (7a) with $y_0=\frac{1}{2}\pi$ ϵ_{RF}^{OPT} then does depend on t and η. The value of ϵ_{RF}^{OPT} is most sensitive to η when the $\frac{1}{2}\pi$ condition is met for $|z_0|$ so small that J_1 is proportional to z_0.

The maximum value of the transition probability can be written:

$$\begin{aligned}(P_0)_{max}&=\{\sin(\tfrac{1}{2}\pi\eta/\eta_T)\}^2, && |\eta|\leq|\eta_T|\,,\\ &=1, && |\eta|\geq|\eta_T|\,.\end{aligned} \tag{10}$$

Since $(P_0)_{max}$ will be much less than unity when $|\eta/\eta_T|\ll 1$, there will be lines with small $|\eta/\eta_T|$ which will be below the noise level in a particular experiment and therefore not detected.

3. Experimental details

The basic molecular beam electric resonance (MBER) apparatus has been described in detail elsewhere [18]. The methods and conditions used for the avoided crossing experiments are very similar to those used in earlier studies of this kind [5–7,12,19]. A rotationally cold beam was produced by expanding a mixture of 4% CH_3CF_3 in argon through a 50 μm nozzle at a backing pressure of 1 bar. The source was

held at room temperature. The velocity of the molecules in the beam was ~550 m/s and the rotational temperature was ~5 K. Commercial gases were used. The beam was monitored at the ion fragment $CH_3CF_2^+$.

The quartz C-field used for OPF_3 [12] was employed. This C-field had two sections with different coatings: a 62 mm long section coated for only ($\Delta m_{TOT}=0$) transitions and a 120 mm long section coated for ($\Delta m_{TOT}=0, \pm 1$) transitions. The former was used for the anticrossing spectra while the latter was used for the dipole measurement and for calibration purposes.

The accuracy of absolute measurements of zero-field energy separations was limited ultimately by the long-term stability and resettability of the voltage source. These were specified to be no larger than 20 ppm. The corresponding limit for relative measurements of small energy difference was 2 ppm set by the short term stability of the voltage source. A detailed discussion of this stability and of the calibration of the electric field has been given earlier [12].

4. Preliminary experiments

4.1. Rotational transitions

In order to determine the rotational constant B and the distortion constants associated with J-dependent terms in eq. (3), mm-wave spectra were obtained with a saturation-modulation absorption spectrometer. A detailed description of this instrument has been given by Kuijpers et al. [20]. The absorption path was 35 cm long and the cell was at room temperature. The ($J=9\leftarrow 8$) and ($J=10\leftarrow 9$) spectra were observed for both $v=0$ and $v=1$. The ($J=11\leftarrow 10$) spectrum was obtained only for $v=0$. The linewidths were 200 kHz, so that the K-splitting could be resolved for the higher K-values, but the σ-splittings could not be resolved. The accuracy of the frequency measurements was ~25 kHz for $v=0$ and ~100 kHz for $v=1$. The results are presented in table 3. Each of these is an average over the three σ-values.

In addition, the ($J=1\leftarrow 0$) transition was observed in the ground torsional state in a conventional MBER experiment in zero external electric field. Here only ($K=0$) is allowed and two distinct σ-levels ex-

Table 3
Frequencies [a] for ($J+1\leftarrow J$) pure rotational transitions in CH_3CF_3 in the ground and first excited torsional states. All entries are in MHz

J	K	Ground state		Excited state	
		observed value	observed − calculated	observed value	observed − calculated
0	0	10370.280(6)	0.006		
8	4	93328.241(30)	0.015	93182.444(100)	−0.038
8	5	93327.909(30)	0.008	93182.067(100)	−0.091
8	6	93327.493(30)	−0.012	93181.760(100)	−0.004
8	7	93327.023(30)	−0.013	93181.285(100)	−0.009
8	8	93326.479(30)	−0.017	93180.770(100)	0.018
9	5	103696.700(25)	0.000	103534.769(100)	0.006
9	6	103696.258(25)	−0.002	103534.328(100)	0.003
9	7	103695.741(25)	0.002	103533.794(100)	−0.009
9	8	103695.140(25)	0.001	103533.207(100)	0.006
9	9	103694.466(25)	0.008	103532.574(100)	0.051
10	5	114065.194(25)	0.001		
10	6	114064.720(25)	0.011		
10	7	114064.138(25)	0.001		
10	8	114063.480(25)	0.004		
10	9	114062.732(25)	0.005		
10	10	114061.881(25)	−0.010		

[a] Each entry is an average over σ, because the σ-splitting was not resolved.

ist. These were not resolved; the result given in table 3 is again an average over σ.

4.2. The electric dipole moment

A precision determination of the electric dipole moment was made by a conventional MBER study of the ($\Delta J=0$, $\Delta m_J=\pm 1$) spectrum. Measurements were carried out for the states $J_K=1_0$, $1_{\pm 1}$, and $3_{\pm 2}$. Each spectrum appeared as a single structureless line with a full width at half height of ~ 15 kHz. The excess broadening over the instrumental line width of 4 kHz was attributed to nuclear hyperfine effects.

Although all the data were consistent, the final value for μ was based on a measurement of a $3_{\pm 2}$ transition. This particular choice was made because the frequency is independent of hyperfine shifts [15] and of the anisotropy in the polarizability. The transition for ($m_J=\mp 1\rightarrow 0$) was measured at 240.97 MHz in an electric field of 1226 V/cm. The field was calibrated with the $(J, m_J)=(1, \mp 1)\rightarrow(1, 0)$ transition for OCS in the ground vibrational state. Table 1 lists the absolute value obtained for the dipole moment of CH_3CF_3 in the $3_{\pm 2}$ state along with the value relative to the OCS moment in the ground vibrational state, which was taken from ref. [21].

5. Stark rotational anticrossings

A series of ($\Delta J=0$) Stark avoided crossings with $(K_\alpha=\pm 2)\leftrightarrow(K_\beta=\mp 1)$ has been studied for each J between 2 and 6. The mixing between levels Λ_α and Λ_β is provided by the distortion dipole moment μ_D as defined in ref. [22]. The torsion–rotation symmetry Γ_{RT} is conserved, as well as σ. Because the operator involved has no nuclear spin part, the nuclear spin quantum numbers $\Lambda^N=(I_T m_T I_F m_F)$ do not change. Since transitions between the two interacting levels are possible only when ($\Delta m_{TOT}=0$), it follows that $\Delta m_J=0$ as well.

The energy level scheme for the anticrossing $(J_\alpha=2,\ K_\alpha=\pm 2,\ m_J^\alpha=\pm 2)\leftrightarrow(J_\beta=2,\ K_\beta=\mp 1,\ m_J^\beta=\pm 2)$ is shown in fig. 1. The three allowed Stark anticrossings are indicated by heavy dots. Consider an electric field ϵ far enough below the lowest of the three crossing fields that each pair of interacting levels is separated by an amount large compared with its

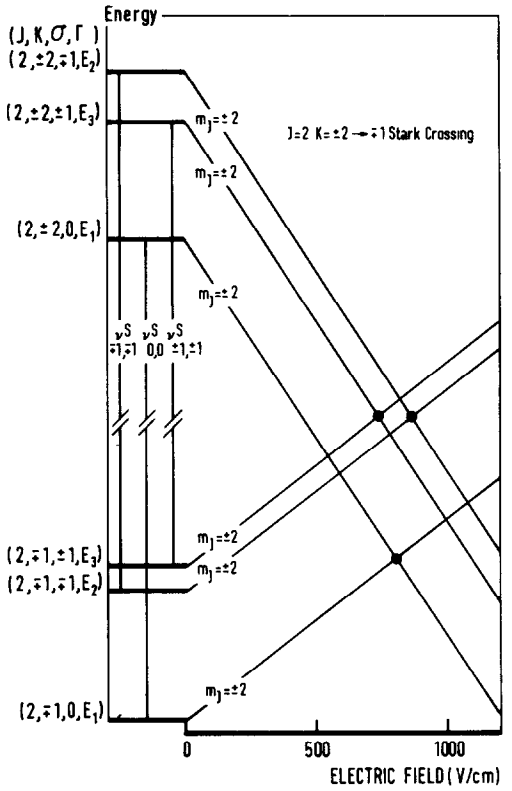

Fig. 1. Schematic plot against the electric field of the energy levels involved in the Stark anticrossing with $J=2$, $K=\pm 2\leftrightarrow\mp 1$, $m_J=\pm 2\leftrightarrow\pm 2$. Upper signs go with upper and lower with lower. The dots indicate the allowed Stark anticrossings; all were observed. With a few simple changes, this plot can also be used for the hyperfine anticrossing with $J=2$, $K=\pm 2\leftrightarrow\pm 1$, $m_J=\pm 1\leftrightarrow\mp 1$; see section 6.1.

minimum separation ν_m that exists at ϵ_c. At such a field, the spectrum will consist of a triplet whose members fall in the same order and with the same separation as they would in the limit $\epsilon\rightarrow 0$. (This is a *normal* spectrum as defined in section 2.B of ref. [12].)

A typical anticrossing spectrum of this type is shown in fig. 2. The triplet is centered at about 1500 kHz. It is almost symmetric with the left hand splitting being a little larger (58 kHz) than the right hand splitting (50 kHz). The three zero-field energy separations can be treated as frequencies and are denoted by $\nu^S_{\sigma_\alpha\sigma_\beta}=\nu^S_{\mp 1,\mp 1}$, $\nu^S_{0,0}$, $\nu^S_{\pm 1,\pm 1}$.

Precision measurements of the absolute crossing field were made of $\nu^S_{\mp 1,\mp 1}$ for $J=2$, 3, 4, 5 and 6 and

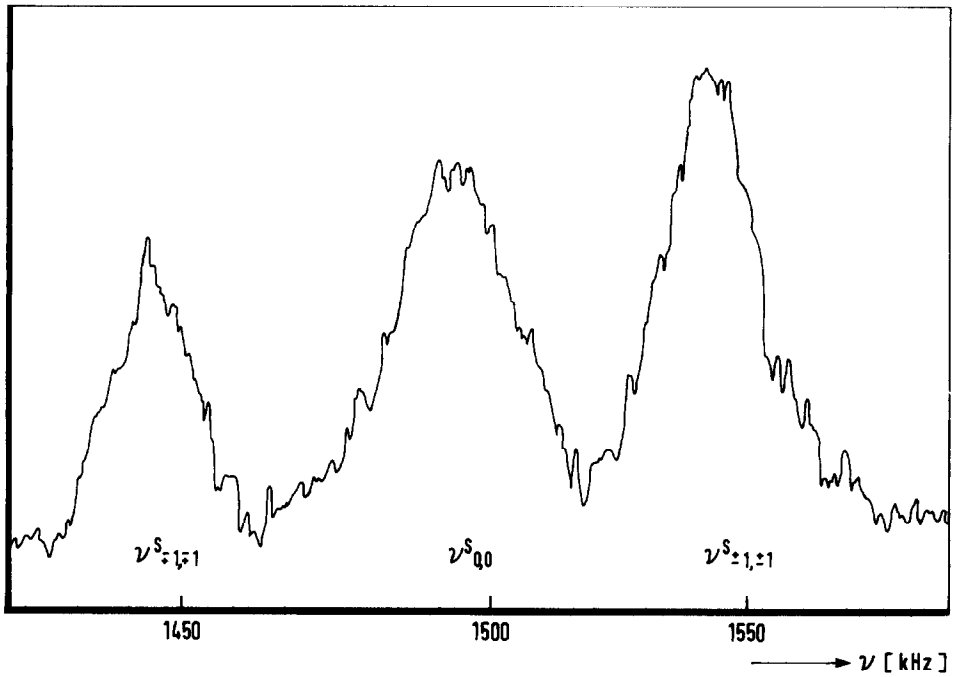

Fig. 2. Spectrum of the Stark anticrossings with $J=2$, $K=\pm 2 \leftrightarrow \mp 1$, $m_J=\pm 2 \leftrightarrow \pm 2$. Each line corresponds to a different torsion–rotation symmetry Γ_{RT}, which is conserved in this type of anticrossing. The splittings have the same values as they would at very low electric fields. The measurement was taken below the crossing in a field of 796.2 V/cm. Eight sweeps were averaged.

Table 4a
Zero-field frequencies in the ground torsional state of CH_3CF_3 determined from absolute anticrossing measurements. All values are in MHz

J	Upper state			Lower state			Label		Observed value	Observed–calculated
	K_α	σ_α	Γ^α_{RT}	K_β	σ_β	Γ^β_{RT}	I [a]	II [b]		
2	± 2	0	E_1	∓ 1	0	E_1	$\nu^S_{0,0}$	Stark	941.154(18)	0.003
2	± 2	∓ 1	E_2	∓ 1	∓ 1	E_2	$\nu^S_{\mp 1,\mp 1}$	Stark	941.202(18)	0.001
3	± 2	∓ 1	E_2	∓ 1	∓ 1	E_2	$\nu^S_{\mp 1,\mp 1}$	Stark	941.172(18)	0.006
4	± 2	∓ 1	E_2	∓ 1	∓ 1	E_2	$\nu^S_{\mp 1,\mp 1}$	Stark	941.125(18)	0.007
5	± 2	∓ 1	E_2	∓ 1	∓ 1	E_2	$\nu^S_{\mp 1,\mp 1}$	Stark	941.066(18)	0.009
6	± 2	∓ 1	E_2	∓ 1	∓ 1	E_2	$\nu^S_{\mp 1,\mp 1}$	Stark	941.998(18)	0.013
1	± 1	0	E_1	0	± 1	E_4	$\nu^H_{0,\pm 1}$	Aa–A1	313.281(10)	−0.012
2	± 1	0	E_1	0	± 1	E_4	$\nu^H_{0,\pm 1}$	Ba–B1	313.274(10)	−0.012
2	± 2	0	E_1	± 1	∓ 1	E_3	$\nu^H_{0,\mp 1}$	Ca–C1	940.706(18)	0.004
2	± 2	0	E_1	0	± 1	E_4	$\nu^H_{0,\pm 1}$	Da–D1	1254.432(24)	−0.004
2	± 2	0	E_1	0	± 1	E_4	$\nu^H_{0,\pm 1}$	Ea–E1	1254.418(24)	−0.018

[a] The first and second subscripts stand for σ_α and σ_β, respectively. The superscripts S and H indicate Stark and hyperfine anticrossings, respectively.

[b] For the hyperfine anticrossings, this provides a cross-reference to fig. 3 and table 5. The capital letters specify the values for states α and β of J, K, and m_J. The lower case letters and the numbers specify the observed frequency and the σ-assignment, respectively.

Table 4b
Internal rotor splittings in the ground torsional state of CH_3CF_3 determined for relative anticrossing measurements. All values are in kHz

Calculated		Key [d]	Observed		Observed – calculated
label [a,b]	value		label [b,c]	value	
Stark: $K=\pm2\leftrightarrow\mp1$					
$\nu^S_{\pm1,\pm1}(J=2)-\nu^S_{0,0}(J=2)$	−57.8	F, Y		−58.3(8)	−0.5
$\nu^S_{\mp1,\mp1}(J=2)-\nu^S_{0,0}(J=2)$	50.9	F, Y		50.2(8)	−0.7
$\nu^S_{\pm1,\pm1}(J=3)-\nu^S_{0,0})J=3)$	−57.8	F, Y		−58.1(8)	−0.3
$\nu^S_{\mp1,\mp1}(J=3)-\nu^S_{0,0}(J=3)$	50.9	F, Y		50.6(8)	−0.3
$\nu^S_{\pm1,\pm1}(J=6)-\nu^S_{0,0}(J=6)$	−57.9	F, Y		−58.1(1.0)	−0.2
$\nu^S_{\mp1,\mp1}(J=6)-\nu^S_{0,0}(J=6)$	51.0	F, Y		50.9(5)	−0.1
$\nu^S_{\mp1,\mp1}(J=5)-\nu^S_{0,0}(J=2)$	−144.1	F, N		−137.8(1.9)	6.3
Hyperfine set A: $J=1$, $K=\pm1\leftrightarrow0$					
$\nu(2)-\nu(1)$	412	U			
$\nu(3)-\nu(1)$	432	U			
$\nu(4)-\nu(1)$	449	T, N	ν(b)−ν(a)	439(10)	−10
		U	ν(c)−ν(a)	825(10)	
$\nu(5)-\nu(1)$	844	U			
		U	ν(d)−ν(a)	854(10)	
$\nu(6)-\nu(1)$	880	U			
		U	ν(e)−ν(a)	887(10)	
Hyperfine set B: $J=2$, $K=\pm1\leftrightarrow0$					
$\nu(2)-\nu(1)$	412	U			
$\nu(3)-\nu(1)$	432	U			
$\nu(4)-\nu(1)$	449	T, N	ν(b)−ν(a)	444(10)	−5
		U	ν(c)−ν(a)	825(10)	
$\nu(5)-\nu(1)$	844	U			
		U	ν(d)−ν(a)	850(10)	
$\nu(6)-\nu(1)$	880	U			
		U	ν(e)−ν(a)	890(10)	
Hyperfine set C: $J=2$, $K=\pm2\leftrightarrow\pm1$					
$\nu(2)-\nu(1)$	36	F, Y	ν(b)−ν(a)	46(10)	10
$\nu(3)-\nu(1)$	391	S, N			
$\nu(4)-\nu(1)$	427	U			
$\nu(5)-\nu(1)$	449	F, S, Y	ν(c)−ν(a)	448(10)	−1
$\nu(6)-\nu(1)$	463	U			
$\nu(7)-\nu(1)$	499	S, N			
$\nu(8)-\nu(1)$	839	F, Y	ν(d)−ν(a)	841(10)	−2
$\nu(9)-\nu(1)$	912	F, Y	ν(e)−ν(a)	899(10)	−13
Hyperfine set D: $J=2$, $K=\pm2\leftrightarrow0$					
$\nu(2)-\nu(1)$	391	Q, N	ν(b)−ν(a)	401(10)	10
$\nu(3)-\nu(1)$	432	Q, N	ν(c)−ν(a)	424(10)	−8
$\nu(4)-\nu(1)$	463	U			
$\nu(5)-\nu(1)$	822	U			
$\nu(6)-\nu(1)$	895	F, N	ν(d)−ν(a)	898(10)	3
Hyperfine set E: $J=2$, $K=\pm2\leftrightarrow0$					
$\nu(2)-\nu(1)$	391	Q, N	ν(b)−ν(a)	399(10)	8
$\nu(3)-\nu(1)$	432	Q, N	ν(c)−ν(a)	418(10)	−14
$\nu(4)-\nu(1)$	463	U			
$\nu(5)-\nu(1)$	822	U			
$\nu(6)-\nu(1)$	895	F, N	ν(d)−ν(a)	889(10)	−6

[a] For the Stark case, this provides a cross-reference to table 4a.
[b] For the hyperfine case, this provides a cross-reference to table 5 and fig. 3.
[c] For the Stark case, no cross-reference is needed here.
[d] This describes the σ-assignment. F – firm; T – tentative; Q – questionable; U – unassigned; S – coincident with Stark anticrossing; Y – yes, included in fit; N – no, not included in fit.

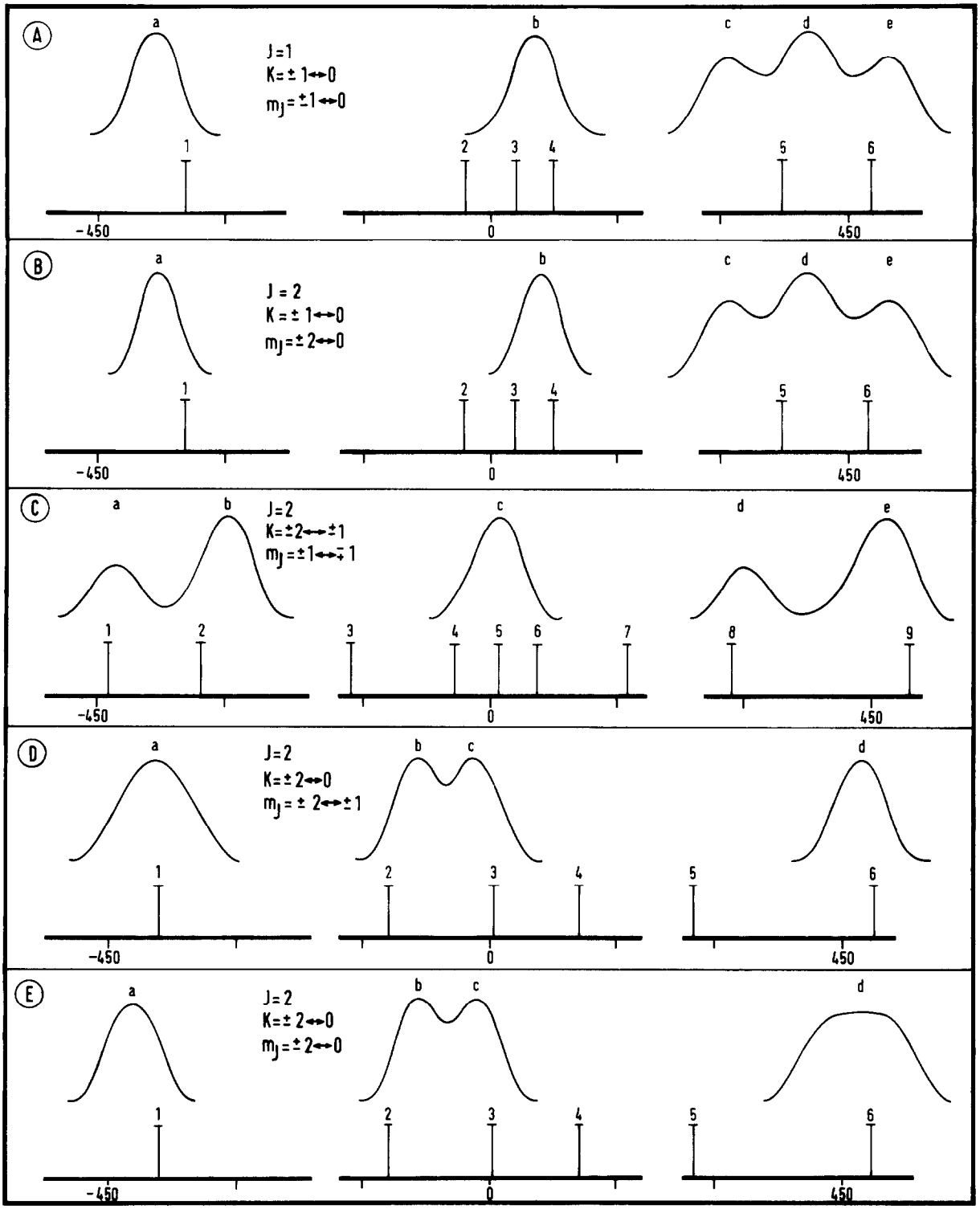

Fig. 3. The observed and calculated spectra for the five sets of hyperfine anticrossings that were studied. For each set, the upper part shows the experimental spectrum (manually smoothed) and the lower section shows the stick spectrum calculated from the torsional splittings using the parameters in table 1. For reference purposes, in each set, the observed lines are labelled a, b, c, ... from left to right and the predicted sticks are labelled 1, 2, 3, ... again from left to right. See table 5 for the σ and Γ_{RT} assignments of the sticks. For the experimental spectra, the vertical scale is constant only within each individual section; it is not the same from section to section within each set, or from one set to the other. For the calculated sticks, the intensities are not represented. The horizontal scale is the same throughout; the tick marks are 50 kHz apart. Within each set, the markers at ±450 kHz show the offsets that apply relative to the central reference.

of $\nu^S_{0,0}$ for $J=2$. Splitting measurements were carried out far from the crossing for $J=2$, 3 and 6. A relative measurement was made of $\nu^S_{\mp 1,\mp 1}$ (for $J=5$) with respect to $\nu^S_{\mp 1,\mp 1}$ (for $J=2$). This was not included in the torsional analysis, but was used to investigate the J-dependence of the dipole moment (see section 8.1). The relative measurements were accurate to $\leqslant 10$ kHz, but the absolute frequencies were limited to ~ 20 kHz by the calibration problem. The measurements are listed in table 4.

6. Hyperfine rotational anticrossings

6.1. Observations and preliminary analysis

Five sets of ($\Delta J=0$) hyperfine avoided crossings have been studied with $J=1$ or 2. Each set can be distinguished by its values of $J_\alpha=J_\beta=J$, $(K_\alpha, m_\alpha)\leftrightarrow(K_\beta, m_\beta)$. For each set, an absolute measurement was made of the zero-field splitting for the lowest frequency member and relative splitting measurements were made for the others. The results are listed in table 4, along with the predicted values (see below).

The five spectra are sketched in fig. 3. Each spectrum is *normal*; i.e., it is taken at a field ϵ far enough below the crossing field that the splittings are the same as they would be for a small electric field. For reference purposes, the five sets are labelled with the capital letters A, B, ..., E. Within each set, the individual lines observed are labelled from low frequency to high with lower case italic letters from a to however many are required.

The energy level scheme is shown in fig. 4 for set A: $(J=1)$, $(\pm 1, \pm 1)\leftrightarrow(0, 0)$. As will be discussed below, each of the six possible anticrossings is allowed by at least one of the nuclear hyperfine interactions. The stick spectrum in fig. 3 shows the frequency splitting among these six as calculated from the torsion–rotation Hamiltonian H_{TR} in eq. (1), using the parameters in table 1. All the sticks are of equal height as no attempt has been made in fig. 3 to represent the calculated intensities. For reference purposes, the sticks predicted are labelled from low frequency to high with 1, 2, ... For each stick, table 5 lists $(K_\alpha, \sigma_\alpha, \Gamma^\alpha_{RT})\leftrightarrow(K_\beta, \sigma_\beta, \Gamma^\beta_{RT})$.

As can be seen from fig. 4, the three possible upper states consist of two ($\sigma_\alpha\neq 0$) levels that are closely

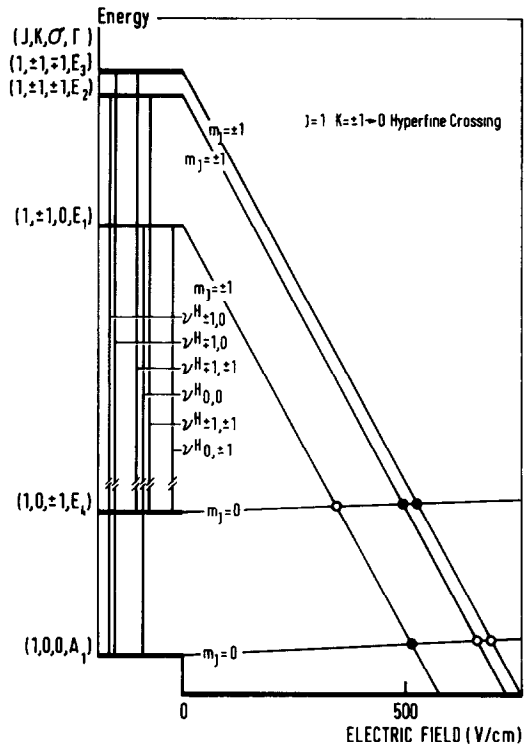

Fig. 4. Schematic plot against the electric field of the energy levels involved in the hyperfine anticrossings with $J=1$, $K=\pm 1\leftrightarrow 0$, $m_J=\pm 1\leftrightarrow 0$. Upper signs go with upper and lower signs with lower. There is one exception: both sign orders for σ in the E_4 level must be considered (see section 6.1). For clarity, the second-order Stark effect of the ($K=0$) states has been exaggerated. The dots indicate the allowed hyperfine anticrossings. See set A in fig. 3, tables 4 and 5.

spaced (~ 35 kHz) and a third ($\sigma_\alpha=0$) level that falls well below (~ 440 kHz). Since the lower state has $K_\beta=0$, there is only one possible energy for $\sigma_\beta\neq 0$. The ($\sigma_\beta=0$) level is well below, again by about 440 kHz. From this energy level structure, the splitting pattern for set A in fig. 3 is easily deduced. It consists of a single low frequency line, a central triplet, and a high frequency doublet. The frequency range spanned by the triplet is the same as that spanned by the doublet, namely ~ 35 kHz. The centre of the triplet is halfway between the singlet and the centre of the doublet. The entire pattern spans ~ 880 kHz.

Fig. 3 and table 5 present parallel information for the other four sets. For each of sets B, D and E, the lower level has $K_\beta=0$ and the upper level has $K_\alpha=\pm 2$

Table 5
Assignments for σ and Γ_{RT}, mixing mechanisms, g-factors, and relative intensities for hyperfine anticrossings

Index [a]		$\tilde{g}$	Upper state		Lower state		η [b]	I_{calc}
calc.	obs.		σ_α	Γ^α_{RT}	σ_β	Γ^β_{RT}		
Set A: $J=1$; $K=\pm1\leftrightarrow0$; $m_J=\pm1\leftrightarrow0$								
1	a		0	E_1	±1	E_4	TF	
					∓1	E_4	TF, TJ	
2			±1	E_2	±1	E_4	TF, FJ	
					∓1	E_4	TF	
3			0	E_1	0	A_2	TF, FJ	
4	b	g_T, g_F	∓1	E_3	∓1	E_4	TF, FJ	
					±1	E_4	TF, TJ	
5	c, d		±1	E_2	0	A_2	TF, TJ	
6	d, e		∓1	E_3	0	A_2	TF	
Set B: $J=2$; $K=\pm1\leftrightarrow0$; $m_J=\pm2\leftrightarrow0$								
1	a	0	E_1	±1	E_4	TF		
				∓1	E_4	TF		
2		±1	E_2	±1	E_4	TF		
				∓1	E_4	TF		
3		0	E_1	0	A_1	TF		
4	b	∓1	E_3	∓1	E_4	TF		
				±1	E_4	TF		
5	c, d	±1	E_2	0	A_1	TF		
6	d, e	∓1	E_3	0	A_1	TF		
Set C: $J=2$; $K=\pm2\leftrightarrow\pm1$; $m_J=\pm1\leftrightarrow\mp1$								
1	a		0	E_1	∓1	E_3	TF	0.62
2	b	g_T+g_F	0	E_1	±1	E_2	TF	2.13
3			±1	E_3	∓1	E_3	TF	1.62
4			±1	E_3	±1	E_2	TF	1.23
5	c	g_T+g_F	0	E_1	0	E_1	TF	5.38
6			∓1	E_2	∓1	E_3	TF	1.23
7			∓1	E_2	±1	E_2	TF	4.17
8	d		±1	E_3	0	E_1	TF	0.62
9	e	g_T+g_F	∓1	E_2	0	E_1	TF	2.13
Set D: $J=2$; $K=\pm2\leftrightarrow0$; $m_J=\pm2\leftrightarrow\pm1$								
1	a	g_T	0	E_1	±1	E_4	TF, TT, TJ	
					∓1	E_4	TF	
2	b		±1	E_3	±1	E_4	TF, FF, FJ	
					∓1	E_4	TF, TT, TJ	
3	c	g_F	0	E_1	0	A_1	TF, FF, FJ	
4			∓1	E_2	∓1	E_4	TF, FF, FJ	
					±1	E_4	TF	
5			±1	E_3	0	A_1	TF	
6	d	g_T	∓1	E_2	0	A_1	TF, TT, TJ	
Set E: $J=2$; $K=\pm2\leftrightarrow0$; $m_J=\pm2\leftrightarrow0$								
1	a	$2g_T$	0	E_1	±1	E_4	TF, TT	4.00
					∓1	E_4	TF	0.38
2	b		±1	E_3	±1	E_4	TF	0.01
					∓1	E_4	TF	0.001
3	c	$2g_F$	0	E_1	0	A_1	TF, FF	8.00
4			∓1	E_2	∓1	E_4	TF, FF	4.00
					±1	E_4	TF	0.38
5			±1	E_3	0	A_1	TF	0.38
6	d	$2g_T$	∓1	E_2	0	A_1	TF, TT	8.00

[a] The calc. index labels the sticks in each set of fig. 3 from left to right. The obs. index labels the observed lines in each set of fig. 3 from left to right. The firmness of the correlation between the two is indicated in table 4b.

[b] This specifies the mechanism responsible for the mixing matrix element η by giving the subscripts on the pertinent operators in eq. (4).

or ± 1. As a result, the energy level scheme and splitting patterns are similar (to a greater or lesser degree) to those of set A. While the details may change, for these four sets, at least the general form of fig. 4 will apply.

However, set C is different in that $K_\beta \neq 0$. Here the general form of fig. 1 can be used. Two modifications must be made. First, $|m_J|$ must be changed from 2 to 1. This implies a decrease by a factor of two in the magnitude of all slopes and a doubling of the crossing field (if the quadratic Stark effect is neglected). Second, upper/lower signs for the α-states couple to lower/upper for the β-states. The zero-field energy levels are *not* altered. *All* intersections correspond to avoided crossings allowed by group theory. The expected splitting pattern (see fig. 3) consists of a low frequency doublet, a central quintet, and a high frequency doublet. The centre of the quintet is halfway between the two doublets and the entire pattern spans about 880 kHz.

Set C is different from the others in another important regard. Three of the sticks in fig. 3 and the corresponding intersections in the modified fig. 1 are Stark-hyperfine hybrids, as defined in ref. [12]. These three are the only ones which conserve Γ_{RT}. They are C3, C5 and C7 (see table 5). Each of the three has $(K_\alpha = \pm 2, \quad \sigma_\alpha, \quad m_J^\alpha = \pm 1) \leftrightarrow (K_\beta = \pm 1, \quad \sigma_\beta = -\sigma_\alpha, \quad m_J^\beta = \mp 1)$, when, as is assumed in table 5, the mixing is provided by nuclear hyperfine interactions. However, the distortion dipole will couple levels $(K_\alpha = \pm 2, \quad \sigma_\alpha, \quad m_J^\alpha = \pm 1) \leftrightarrow (K_\beta = \mp 1, \quad \sigma_\beta = \sigma_\alpha, \quad m_J^\beta = \pm 1)$. As presented here, the α-states for the hyperfine and Stark cases are the same, but the β-states are different. If it were not for the nuclear spin quantum numbers, the Stark state would be related to its hyperfine counterpart simply by simultaneously changing the signs of K_β, σ_β and m_J^β, a step which does not alter the torsion–rotation energy or the Stark energy. In zero magnetic field, the two β-states are degenerate and the effective Hamiltonian provides a 4×4 problem. As the B-field is increased, this reduces to two distinct 2×2 problems. See fig. 2 of ref. [12]. Because the mixing due to the distortion dipole is much larger than that due to the hyperfine terms, the lines for $B = 0$ can be considered to be Stark in nature. Although such lines were observed for C3, C5 and C7, only the observed central component (line Cc) is shown in fig. 3; the other two have been omitted to simplify the diagram.

For each hyperfine anticrossing, the particular nuclear hyperfine terms that can provide the mixing are listed in table 5. Sets A and D can involve spin–rotation interactions since $|\Delta m_J| = 1$, where the others are restricted to dipolar coupling since $|\Delta m_J| = 2$. Sets D and E can involve H_{TT} and H_{FF} since $|\Delta K| = 2$, but the others cannot since $|\Delta K| = 1$. The top–frame dipolar interaction is effective in all cases.

For each case where $K_\beta = 0$ and $\Gamma_{RT}^\beta = E_4$, there are two possible values for σ_β, namely ± 1 or ∓ 1. In these cases, it is possible that there will arise multi-level systems that cannot be treated as a series of distinct two-level systems. If it were possible to neglect H_{TF}, then all such multi-level systems would reduce to two-level problems when a magnetic field is applied (e.g. line A4). However, if all the mixing matrix elements must be taken into account, then three-level systems occur which cannot be reduced.

By assuming that a two-level treatment is adequate, it is possible to predict by using the methods of [9] the relative intensities of the different sticks within a given set, provided that only the dipolar interactions enter. These calculations have been done for sets C and E. The three factors forming the right hand side of eq. (5) were first calculated to get the mixing matrix element η for each magnetic component. The relevant structural parameters were determined from ref. [23]. It was then assumed that ϵ_{RF} was optimized for the particular magnetic component and eq. (10) was used to calculate the corresponding transition probability. The probabilities contributing to the anticrossing in question were then summed to give the results listed as I_{calc} in table 5.

The need for a weighted average over the magnetic components (rather than simply a sum) must be considered since in principle ϵ_{RF}^{OPT} can be different for the individual magnetic components (see section 2.3). Fortunately, this complication did not arise here. If $|\eta| < |\eta_T|$, ϵ_{RF}^{OPT} depends only on $\Delta\mu_{\alpha\beta}$ and ν_0 and so is (to excellent approximation) the same for all components of the same stick. If $|\eta| > |\eta_T|$, and all components have the same η, then again all components can be optimized at once. All the sticks in fig. 3 fall into one or other of these two categories.

One result that becomes apparent in calculating the intensities I_{calc} in table 4 is that the matrix elements of H_{TF} are much larger in magnitude for $\Delta K = \pm 1$ than for $\Delta K = \pm 2$. A large part of the reason for this differ-

ence can be seen from eq. (59) of [9]. Let us define the "length" of the molecule to be the distance between the hydrogen and fluorine planes. Let us also define the "diameter" of the molecule to be the sum of the hydrogen and fluorine distances from the symmetry axis. Then, roughly speaking, the magnitude of the ratio of the ($\Delta K = \pm 1$) and ($\Delta K = \pm 2$) matrix elements of H_{TF} will contain a factor equal to the molecular length divided by a fraction of the molecular diameter. For $\Delta K = \pm 2$, the values of $|\langle H_{TF} \rangle|$ are so small compared to those of $|\langle H_{TT} \rangle|$ and $|\langle H_{FF} \rangle|$ that the TF contribution is negligible in cases where another dipolar interaction contributes. This fact has been used in generating I_{calc} in table 4. On the other hand, the I_{calc} for TF with $\Delta K = \pm 1$ are of the same order as the I_{calc} for TT and FF with $\Delta K = \pm 2$.

Since $\Delta m_J \neq 0$ for all the hyperfine anticrossings, each anticrossing is magnetically active. Thus when a magnetic field is applied, each stick in fig. 3 splits into at least one pair of lines. Each such pair has a separation given in Hz by $2(\mu_N/h)B|g_{eff}|$ where μ_N is the nuclear magneton and the effective g-factor g_{eff} is defined by eq. (19) of [12]. It is often convenient to approximate g_{eff} by its dominant nuclear terms:

$$\tilde{g} = g_T \Delta m_T + g_F \Delta m_F . \qquad (11)$$

Here g_T and g_F are, respectively, the nuclear g-factors for the spins in the top and in the frame. There will be one pair for each possible combination $|\Delta m_T|$, $|\Delta m_F|$. By measuring $\tilde{g}$, it is possible to determine the magnetic selection rules for the pair in question.

Magnetic studies carried out for selected lines in sets A, C, D and E. The positive results found are listed in table 5. These should be interpreted only as indicating the dominant selection rules. Since lines with small $|\eta/\eta_T|$ can disappear into the noise (see section 2.3), the experimental evidence shows that the other possibilities are *either* forbidden *or* are associated with much smaller mixing matrix elements.

6.2. Assignments

From a comparison of the observed and predicted spectra in fig. 3 along with the intensities in table 5, it is clear that the assignment poses some serious difficulties. The first question to be addressed is the magnitude of the contributions to the zero-field energies from the diagonal matrix elements of the nuclear hyperfine interactions. Let us compare sets A and B. The values of J are different. The values of $|\Delta m_J|$ are different: set B can derive its mixing only from H_{TF}, while set A involves the spin–rotation interaction as well. (See table 5.) The diagonal hyperfine contributions will also be different. Yet the two spectra are virtually identical. From table 4, the splitting measurements differ by between 0 and 5 kHz. This similarity is not surprising if only torsion–rotation effects enter, because these are independent of m_J and, to excellent approximation, of J. (Compare the stick spectra in fig. 3.) A comparison between sets D and E yields similar results with respect to both the expected hyperfine differences and the similarities in the observed spectra. Although the close matching of the frequencies of set A with B and of the set D with E may be fortuitous, it constitutes very strong evidence that the nuclear hyperfine shifts from diagonal matrix elements are less than 10 kHz in magnitude.

The second question to be addressed is the level of consistency that can be expected (in the absence of hyperfine shifts) when comparing absolute frequency measurements. From fig. 3, $\nu(A1) - \nu(B1) = 0$ and $\nu(D1) - \nu(E1) = 0$. From table 4a, $\nu(Aa) - \nu(Ba) = 7$ kHz and $\nu(Da) - \nu(Ea) = 14$ kHz. The corresponding errors from the 20 ppm upper limit on the drift etc. of the voltage source are 14 and 34 kHz. It will therefore be assumed here that the level of consistency to be expected for absolute measurements is 10 ppm. This limit is in agreement with that observed in OPF_3 [12] where 7 ppm was measured using the same apparatus.

With limits of 10 kHz and 10 ppm, respectively, on hyperfine shifts and voltage uncertainty, combination differences can be used to test various assignments. Such combination differences can be found because there are spectra for $K = \pm 2 \leftrightarrow 0$, $K = \pm 1 \leftrightarrow 0$ and $K = \pm 2 \leftrightarrow \pm 1$. Consider stick C5 as an example. From the stick assignments in table 5, it follows that $\nu(C5)$ can be expressed as $\nu(E1) - \nu(B1)$; $\nu(D1) - \nu(A1)$; $\nu(E1) - \nu(A1)$; $\nu(D1) - \nu(B1)$. To each stick, the best experimental frequency was assigned and the four combination differences were calculated. Each combination difference was subtracted from $\nu(Cc)$ (which has been assigned to C5) to generate what shall be called the loop defect. Finally, the mean loop defect and its rms deviation were calculated. Two such combination difference tests

Table 6
Combination differences for the zero-field frequencies of the hyperfine anticrossings [a]

Index [b]			mean loop defect [d] (kHz)
reference	example [c] of combination difference		
	upper line	lower line	
C1–Ca	E1–Ea	B4–Bb	-1 ± 8
C1–Ca	E3–Ec	B6–Bd	-11 ± 14
C2–Cb	E1–Ed	B2–Bb	46 ± 8
C2–Cb	E3–Ec	B5–Bc	8 ± 13
C5–Cc	E1–Ea	B1–Ba	6 ± 9
C5–Cc	E3–Ec	B3–Bb	27 ± 12
C8–Cd	E2–Eb	B1–Ba	-2 ± 11
C8–Cd	E5–Ed	B3–Bb	-53 ± 14
C9–Ce	E4–Ec	B1–Ba	36 ± 13
C9–Ce	E6–Ed	B3–Bb	5 ± 14

[a] For a discussion of the first entry for C5–Cc as an example, see section 6.2.
[b] The first part of each index (e.g. C1) specifies the quantum numbers and the second part (e.g. Ca) labels the experimental frequency. See table 5 and fig. 3.
[c] For each reference, there are four possible combination differences. Only one is listed here.
[d] The loop defect is the reference frequency minus the combination difference.

could be carried out for each of the five lines in set C. The results are given in table 6. The rms deviations in the loop defects are consistent with the 15 kHz value expected from the 10 ppm voltage uncertainty. Any mean loop defect that differs from zero by more than 15 kHz indicates that at least one assignment in the loop is incorrect.

From fig. 3 and tables 4–6, several assignments can be made. First, line Cc can be taken as C5 since this is coincident with the Stark anticrossing. Second, the identifications of lines Aa, Ba, Da and Ea are unambiguous. In each case, only one line is predicted and only one observed. Furthermore, the first C5 loop involves only these 4 lines and Cc; the loop defect is small (6.3 kHz). Third, the assignments of Ca, Cb, Cd and Ce as shown in table 5 are firm. These are consistent with the combination differences, although this type of evidence is strong only for Ca. The intensity calculations predict that each doublet should have its stronger member on the high frequency side and that the two doublets have the same weak/strong intensity ratio. The observations agree with these predictions. Fourth, Ed must correspond to E6. The alternative assignment leads to a very large loop defect and would involve a much weaker anticrossing ($I_{calc}=0.38$ as against 8.00). It follows then that Dd corresponds to D6.

Several other *tentative* conclusions can be drawn. First, line Bb is dominated by stick B4, with perhaps a small amount of pulling by stick B3. Second, the triplet Bc, Bd, Be together corresponds to the predicted doublet B5, B6. Similar statements can be made about set A.

Each g-factor $\tilde{g}$ measured is consistent with the assignments made and the mixing mechanisms deduced. See table 5. Three points in particular should be mentioned. First, the entire set C is predicted to derive its mixing from H_{TF}. This has been confirmed. Second, line Ed goes with $2g_T$. This confirms that Ed arises from E6 and not from E5, which goes with g_T+g_F. Third, line Ec goes with $2g_F$. This shows that Ec can be assigned to E3 or E4, but not to E2, which goes with g_T+g_F.

However, two puzzles remain. First, the sticks A5 and A6 form a doublet with a torsion–rotation splitting of 36 kHz, while the observations consist of a triplet Ac, Ad and Ae which spans a frequency region $[\nu(\mathrm{Ae})-\nu(\mathrm{Ac})]$ of ~ 64 kHz. The same statement applies to set B. From refs. [9] and [12], it is easily shown that the diagonal matrix elements of the hyperfine interactions (alone) cannot be responsible for the extra splitting. In particular, the magnitude of the splitting and the close similarity of the two triplets pose serious difficulties in this regard.

The second puzzle is associated with the observed doublet Eb, Ec. From combination differences and the g-factors, line Ec must be associated with stick E3 (E2 and E4 can be excluded). The fact that E4 appears to be missing in spite of the high intensity can always be attributed to "apparatus effects". However, line Eb seems to correspond to E2. This assignment is difficult to accept. Stick E2 has a very small intensity and the corresponding anticrossings in CH_3SiF_3 could not be observed; see ref. [6] and row 3 of table XIV in ref. [9]. It is conjectured that both Eb and Ec correspond to E2, with the additional splitting provided by the same mechanism as is operating for the triplets in sets A and B. Similar arguments apply to set D.

If the conjecture above is correct, then both the doublet puzzle and the triplet puzzle involve the levels with ($K_\beta=0$, $\sigma_\beta=0$). In this case, the addition of some J-independent interaction involving the nuclear spin and possibly the torsion might explain the observations.

Another explanation is also being considered. In CH_3CF_3 some of the splittings between the torsional states are only a factor ~ 10 larger in magnitude than the expected hyperfine matrix elements η which break the torsion–rotation symmetry. For example, the two energy levels in fig. 4 are separated by ~ 35 kHz, while the matrix element of H_{FF} which couples the levels is ~ 2 kHz (see row 8 of table XIV in ref. [9]). It may be that this mixing plays a role in the crossings.

7. Torsion–rotation analysis

A least squares analysis of the data set was carried out using the torsion–rotation Hamiltonian given in eqs. (1), (2) and (3). The data set consisted of the rotational frequencies in table 3 and a selection of the zero-field splittings in table 4. The Stark anticrossing component included all the absolute and splitting measurements except the difference $[\nu^S_{\mp 1,\mp 1}(J=5)-\nu^S_{\mp 1,\mp 1}(J=2)]$. The hyperfine anticrossing components included absolute measurements of the first line in each set and splittings for all the other lines in set C. This accounts for all the definite assignments discussed in section 6.2, except lines Dd and Ed. These two were omitted in the final fit because the large width of Ed in particular made it difficult to determine the frequency to the desired accuracy. In fact, the results did not change significantly when these two were included. All the zero-field splittings were determined from the crossing fields using methods discussed earlier [5,24]. The dipole moment was held fixed (for all J and K) at the value given for μ in table 1.

The final set of parameters is given in table 1. The differences between the observed and calculated values are listed in tables 3 and 4. From these residuals and the comparison in fig. 3 between the stick spectra and the observed spectra, it is clear that the agreement is very good. There is clearly insufficient information to fit a further parameter.

The most important constants fixed at zero in the fit were F_{3K}, D_{Km}, D_{Jm} and D_K. The effects of F_{3K} and D_{Km} have been absorbed into A^{eff}. This (rather than A) has been used to determine F and hence V_3. This provides one of the reasons that only an effective barrier height can be found here. The effect of D_{Jm} has been absorbed into F_{3J}^{eff} (see refs. [5] and [10]). The neglect of D_K decreases the value of A^{eff} by ~ 10 kHz. The constants fixed at zero cannot account for the puzzles noted in section 6.2.

From A^{eff} and ρ, the moment of inertia I_α of the methyl top has been determined to be 3.21(4) amu Å^2. This can be compared with 3.170(2) amu Å^2 for CH_3SiF_3 [6]. The difference between the two values of I_α is less than the error. The uncertainty in I_α for CH_3CF_3 is much bigger, in large part because the torsional splittings are much smaller. A similar statement can be made with regard to V_3^{eff} and ρ.

8. Related studies

8.1. The J-dependence of the dipole moment

It is well known [25,24] that for ($\Delta J=0$) matrix elements the effective dipole moment

$$\mu(JK)=\mu_0+\mu_J J(J+1)+\mu_K K^2\,, \qquad (12)$$

where μ_0 is the equilibrium moment (except for a small correction), while μ_J and μ_K are distortion dipole constants. The present measurements are insensitive to μ_K; it is not considered further. However, using methods discussed earlier [12,6], it is possible to evaluate μ_J.

In principle it is possible to determine μ_J from the absolute measurements of $\nu^S_{\mp 1,\mp 1}$ given in table 4. As J increases from 2 to 6, the differences (observed – calculated) show a clear trend, which results [6,12] from the fact that μ_J has been neglected in section 7. Unfortunately the trend is not significant if we take the level of consistency of the voltage source for absolute measurements to be 10 ppm (9 kHz), as discussed in section 6.2.

On the other hand, the relative measurement $[\nu^S_{\mp 1,\mp 1}(J=5)-\nu^S_{\mp 1,\mp 1}(J=2)]$ is limited to 2 ppm (2 kHz) by the short-term stability of the voltage source. This has sufficient accuracy to determine μ_J. From eq. (4) of ref. [6],

$$\nu^{S}_{\mp 1,\mp 1}(K=5) - \nu^{S}_{\mp 1,\mp 1}(J=2) = -72[D_{JK} + (A-B)\mu_J/\mu_0] . \quad (13)$$

The term ρ^2 in eq. (4c) of ref. [6] has been neglected because it is not significant here. The values of D_{JK}, $(A-B)$ and μ_0 have already been determined. The value of μ_J obtained from eq. (13) is listed in table 1. This result can be compared to the value [6] of 1.23(26) μD for CH_3SiF_3.

The determination of μ_J here is uncorrelated with the determinations of the other parameters. It has therefore been possible to fix μ_J at zero in the other studies carried out.

8.2. The distortion dipole moment

For a C_{3v} symmetric rotor like OPF_3, the minimum separation ν_m between the interacting levels in a Stark anticrossing $(J, K_\alpha = \pm 2, m^\alpha_J = \pm J) \leftrightarrow (J, K_\beta = \mp 1, m^\beta_J = \pm J)$ is given by [12]

$$\nu_m = \mu_D \epsilon_c J[(J-1)(J+2)]^{1/2}. \quad (14)$$

When the change is made to a molecule like methyl silane, this one anticrossing goes over into three, one for each possible Γ_{RT}. However, eq. (14) can be applied to each of the three individually provided the distortion dipole moment μ_D is re-interpreted and allowed to depend on σ [22]. In the high barrier limit, the σ-dependence should vanish, but μ_D still includes a torsional contribution; see eq. (17) of ref. [22].

In CH_3CF_3 for $J=6$, the value of ν_m is large enough that anticrossing spectra can be measured, even when $\epsilon = \epsilon_c$ and the resonance frequency is ν_m itself. Fig. 5 shows a typical spectrum for $\Gamma_{RT} = E_2$ taken within two linewidths of ν_m. For each Γ_{RT}, measurements were made well below, near and well above the crossing. The results were analysed using the standard equations for a two-level anticrossing system [12].

The value of ν_m was independent of Γ_{RT} to within the experimental accuracy of 0.5%: the results were 114.46(64), 114.16(57) and 114.39(81) kHz for $\Gamma_{RT} = E_1$, E_2 and E_3, respectively. Thus to this level of accuracy, it is confirmed that μ_D is independent of σ. The weighted average for ν_m of 114.31(38) kHz was used to obtain the value of μ_D given in table 1. The corresponding value for CH_3SiF_3 is 2.13(57) μD [6].

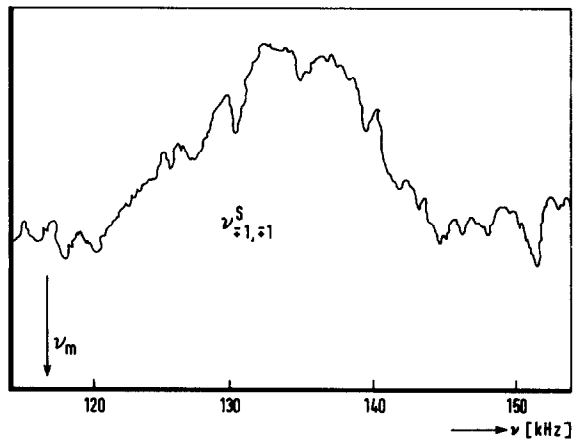

Fig. 5. Spectrum for the Stark anticrossing with $J=6$, $K = \pm 2 \leftrightarrow \mp 1$, $\sigma = \mp 1 \leftrightarrow \mp 1$, $m_J = \pm 6 \leftrightarrow \pm 6$ taken with the field just below the crossing value. The value of the minimum separation $\nu_m = 114.8(1.0)$ kHz is indicated.

8.3. The rotation g-factors

Conventional MBER spectroscopy can be used to determine the magnitude and relative sign of the rotational g-factors parallel and perpendicular to the symmetry axis [15]. These are represented by $g_\parallel$ and $g_\perp$, respectively, in units of the nuclear magneton μ_N. With a magnetic field $\boldsymbol{B}$ parallel to the electric field, each line in the $(\Delta J=0, \Delta m_J = \pm 1)$ Stark spectrum splits into two lines separated by $2(\mu_N/h)B|g_{JK}|$ Hz, where

$$g_{JK} = g_\parallel + (g_\parallel - g_\perp)K^2/J(J+1) . \quad (15)$$

The effects due to nuclear shielding are negligible here. Such Zeeman splittings were measured for $J_K = 1_0$, $3_{\pm 1}$ and $3_{\pm 3}$ in a field of 820 mT. It was found that $g_{1,0} = 0.01774(10)$, $g_{3,1} = 0.0193(2)$, and $g_{3,3} = 0.0214(2)$. From these values, the values of $|g_\parallel|$ and $|g_\perp|$ were found and it was shown that $g_\parallel/g_\perp > 0$. The results are given in table 1.

Avoided crossing MBER spectroscopy can be used to determine the absolute signs of the rotational g-factors [4,12]. As discussed in section 6.1, with $\boldsymbol{B}$ parallel $\boldsymbol{\epsilon}$, the anticrossing spectrum consists of pairs of lines split by $2(\mu_N/h)B|g_{eff}|$. For the anticrossing corresponding to stick C5 in fig. 4, it can be shown from eq. (19) of [12] that

$$g_{eff} = g_T + g_F - g_R , \quad (16)$$

where

$$g_R = 2[g_\perp + \tfrac{5}{12}(g_\parallel - g_\perp)]\,. \qquad (17)$$

A measurement made with $B = 40$ mT led to the result that $g_{eff} = 10.8893(40)$ nm. From the known values for the nuclear g-factors [26], it follows that $g_R = -0.191(15)$ nm. From the results of the conventional study (see table 1), $g_R = \pm 0.197(2)$ nm. The agreement for $|g_R|$ is excellent. Furthermore, the negative sign for g_R shows that both $g_\parallel$ and $g_\perp$ are negative, as shown in table 1.

9. Discussion

The molecular beam avoided crossing method has been applied to the determination of the leading torsional parameters of a symmetric rotor (CH_3CF_3) for which the largest internal rotor splitting in the ground vibronic state are $\leqslant \frac{1}{2}$ MHz. By using combination differences, selection rules, relative intensity calculations, and Zeeman studies, a detailed investigation has been carried out of the hyperfine rotational anticrossings. On the one hand, the frequency shifts due to the diagonal hyperfine matrix elements have been shown experimentally to be less than 10 kHz in magnitude. It has been possible for several anticrossings to make definite assignments of the torsion–rotation symmetries Γ^α_{RT} and Γ^β_{RT} for the two interacting levels. The corresponding zero-field splittings have then been used to help evaluate V_3^{eff} and I_α. On the other hand, for several $(\Gamma^\alpha_{RT}, \Gamma^\beta_{RT})$ no definite assignments were possible. In some of the cases, anomalous spectral features appeared which could not be explained in terms of the diagonal matrix elements of the torsion–rotation nuclear spin Hamiltonian.

In the current work, considerable attention has been paid to the breaking of the torsion–rotation symmetry Γ_{RT} near the crossing region by the nuclear hyperfine terms. However, in some cases, these same terms will produce interesting effects in zero field. Consider a molecule with the same torsion–rotation energies as CH_3CF_3, but with hyperfine matrix elements off diagonal in Γ_{RT} which are a factor of 10 or more larger, as might arise from a quadrupole interaction. Then, in zero field Γ_{RT} would no longer be a good quantum number and the energy levels would have to be calculated by diagonalizing the full Hamiltonian. A similar situation arises in tetrahedral molecules [27,28]. In that case, the rotational symmetry Γ_R is a good quantum number only so long as the splittings produced by the tensor distortion interactions dominate the symmetry-breaking terms in the nuclear hyperfine Hamiltonian. Thus, at low values of J, Γ_R is a good quantum number in CH_4, but not in CF_4. These effects have been studied at length in connection with level clustering in spherical tops [29–31].

Acknowledgements

The authors wish to express their appreciation to Dr. J.T. Hougen for many lengthy discussions and for his invaluable assistance with the relative intensity calculation. The authors wish to thank Dr. A. Dymanus for many helpful suggestions and Dr. P.J.M. Kuijpers for his assistance in obtaining the mm-wave data. One of us (I.O.) wishes to acknowledge gratefully the support of the Natural Sciences and Engineering Research Council of Canada. Both authors would like to thank the North Atlantic Treaty Organization Grant Program for its assistance through travel grant No. 1454.

References

[1] W. Gordy and R.L. Cook, Microwave Molecular Spectra, 3rd Ed., in: Techniques of Chemistry, ed. A. Weissberger, Vol. 18 (Wiley, New York, 1984).
[2] J.K.G. Watson, J. Mol. Spectry. 40 (1971) 536.
[3] M.R. Aliev and V.M. Mikhaylov, J. Mol. Spectry. 49 (1974) 18.
[4] W.L. Meerts and I. Ozier, Phys. Rev. Lett. 41 (1978) 1109.
[5] W.L. Meerts and I. Ozier, J. Mol. Spectry. 94 (1982) 38.
[6] W.L. Meerts and I. Ozier, Chem. Phys. 71 (1982) 401.
[7] I. Ozier and W.L. Meerts, Can. J. Phys. 62 (1984) 1844; ibid. 63 (1985) 1375.
[8] W.L. Meerts, I. Ozier and J.T. Hougen, J. Chem. Phys. 90 (1989) 4681.
[9] J.T. Hougen, W.L. Meerts and I. Ozier, J. Mol. Spectry., to be published.
[10] M. Wong, I. Ozier and W.L. Meerts, J. Mol. Spectry. 102 (1983) 89.
[11] N. Moazzen-Ahamadi, I. Ozier and H. Jagannath, J. Mol. Spectry. 119 (1986) 299.
[12] I. Ozier and W.L. Meerts, Can. J. Phys. 59 (1981) 150.
[13] P.R. Bunker, Mol. Phys. 9 (1965) 257.

[14] N. Moazzen-Ahmadi, I. Ozier and W.L. Meerts, J. Mol. Spectry. 137 (1989) 166.
[15] W.L. Meerts, I. Ozier and A. Dymanus, Can. J. Phys. 57 (1979) 1163.
[16] N.F. Ramsey, Molecular Beams (Oxford Univ. Press, Oxford, 1956).
[17] M.A. Abramowitz and I.A. Stegun, Handbook of Mathematical Functions (Dover, New York, 1972).
[18] F.H. de Leeuw and A. Dymanus, J. Mol. Spectry. 48 (1973) 427;
F.H. de Leeuw, Thesis, Katholieke Universiteit, Nijmegen, Netherlands (1971).
[19] W.L. Meerts and I. Ozier, J. Chem. Phys. 75 (1981) 596.
[20] P.J.M. Kuijpers, T. Törring and A. Dymanus, Z. Naturforsch. 30a (1975) 1256.
[21] J.M.L.J. Reinartz and A. Dymanus, Chem. Phys. Letters 24 (1974) 346.
[22] N. Moazzen-Ahmadi and I. Ozier, J. Mol. Spectry. 126 (1987) 99.
[23] L.F. Thomas, J.S. Heeks and J. Sheridan, Z. Electrochem. 61 (1957) 935.
[24] I. Ozier and W.L. Meerts, J. Mol. Spectry. 93 (1982) 164.
[25] J.K.G. Watson, M. Takami and T. Oka, J. Chem. Phys. 70 (1979) 5376.
[26] G.H. Fuller, J. Phys. Chem. Ref. Data 5 (1976) 835.
[27] C.H. Anderson and N.F. Ramsey, Phys. Rev. 149 (1966) 14.
[28] P.Y. Yi, I. Ozier and C.H. Anderson, Phys. Rev. 165 (1968) 92.
[29] A.J. Dorney and J.K.G. Watson, J. Mol. Spectry. 42 (1972) 135.
[30] W.G. Harter and C.W. Patterson, Phys. Rev. Letters 38 (1977) 224; ibid., J. Chem. Phys. 80 (1984) 4241.
[31] J. Bordé and Ch. Bordé, Chem. Phys. 71 (1982) 417.